



Orbital Debris

Quarterly News

Volume 29, Issue 1
February 2025

Inside...

Radar Measurements of the Orbital Debris Environment from HUSIR and Goldstone: 2023	4
Meeting Reports	7
Monthly Number of Objects in Earth Orbit by Object Type	8
Upcoming Meetings	9
Space Missions and Satellite Box Score	9

Two New On-orbit Fragmentations

The U.S. Space Forces - Space (S4S) identified two new on-orbit fragmentations and made the announcements via the space-track website over the past quarter.

The first breakup was an Atlas V Centaur (International Designator 2018-022B, U.S. Satellite Catalog Number 43227) on 6 September 2024. The 2.2-metric-ton upper stage was associated with the deployment of National Oceanic and Atmospheric Administration (NOAA) Geostationary Operational Environmental Satellite (GOES) 17 on 1 March 2018. After releasing the GOES-17 spacecraft, the Centaur successfully maneuvered to a medium Earth orbit (MEO) disposal orbit. At the time of the breakup, the apogee and perigee altitudes of this Centaur were approximately 34,949 km and 7622 km, respectively, with an inclination of 9.3 degrees. Although more than 10 fragments were initially identified, none had been cataloged by the S4S as of 13 January 2025. The breakups of two

other Centaurs with similar MEO disposal orbits were reported by the S4S in August 2018 (2014-055B, 109 cataloged fragments, see ODQN vol. 22, issue 4, November 2018, p. 2 and ODQN vol. 23, issues 1&2, May 2019, p. 2) and April 2019 (2018-079B, 214 cataloged fragments, see ODQN vol. 23, issue 3, August 2019, pp. 1-2). It is likely that the cause of the breakups was related to passivation.

The second breakup was associated with Intelsat 33E (International Designator 2016-053B, U.S. Satellite Catalog Number 41748) in geosynchronous orbit (GEO) at approximately 04:30 UTC on 19 October 2024. At the time of the breakup, the apogee and perigee altitudes of Intelsat 33E were 35,797 km and 35,773 km, respectively, with an inclination of 0.037 degree. Intelsat 33E was launched in 2016 and was still operational when the breakup occurred. The S4S had cataloged 18 fragments from the breakup as of 13 January 2025. ♦

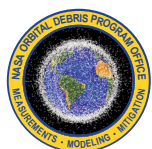
PROJECT REVIEW

Machine Learning Applications Supporting the ODPO

A. MANIS, B. BUCKALEW, M. LAMBERT,
J. MELO, C. CRUZ, AND H. COWARDIN

The NASA Orbital Debris Program Office (ODPO) is investigating the feasibility of machine learning (ML) to process large data sets for efficiency and minimize human-in-

the-loop processes. Several projects and data products used by the NASA ODPO involve large amounts of complex data and are prime candidates for ML applications, including imagery and numerical data from DebrisSat, optical images from the Eugene Stansberry-



A publication of the
NASA Orbital Debris
Program Office (ODPO)

continued on page 2

ML Applications

continued from page 1

Meter Class Autonomous Telescope (ES-MCAT), and radar data from the Haystack Ultrawideband Satellite Imaging Radar (HUSIR) and the Goldstone Orbital Debris Radar System.

One of the premier projects to feature a vast amount of data is the DebrisSat project. This hypervelocity impact experiment was designed to simulate a catastrophic collision and breakup of a modern-day low Earth orbit spacecraft to characterize fragmentation debris and update engineering and environmental models (ODQN vol. 28, issue 4, October 2024, pp. 5-8). To date, DebrisSat has generated close to 300,000 fragments of size 2 mm and larger. These are individually isolated and extracted from the soft-catch foam panels and characterized to determine the material, size, and mass, which are also used to derive quantities such as volume, average cross-sectional area, and area-to-mass ratio. With the large amount of imagery and numerical data needed to complete this process, two specific opportunities for applying ML to the DebrisSat project have been investigated.

The first application is a feasibility study focused on minimizing the need to extract all fragments embedded in the soft-catch panels; the project is focused on characterizing fragments that can be used to update the various models and completing the process within a limited time frame. The non-ML process currently in place within DebrisSat uses x-ray scanning imagery to identify fragments, determine each fragment's location within the imagery file, and estimate the size to determine if the fragment should be extracted or not. Once extracted, the fragment's

material can be assessed – though assessment is complicated and subject to human error when determining what material is most dominant in the fragment. It is especially difficult to distinguish fragments of aluminum, stainless steel, and titanium, which may appear visibly identical and thus are generally characterized as generic “metal” until the specific material can be identified later in the characterization process. The proposed approach for ML application to address this problem is to utilize the imaged color gradients produced by the scanner while the fragments remain embedded in the soft-catch foam. Using “random forest classifier” methodology, the red-green-blue color components and the shape of each fragment were used to train the application to identify the material type and shape and to reproduce the prior results for location and size. The results were promising with this first approach, indicating excellent material identification for titanium – 100% in the test case – with other materials having various levels of success provided the limited dataset used for this feasibility study. Identifying the appropriate material type continues to be challenging, but investing in ML appears to be a viable path, provided an appropriate training dataset can be identified and implemented. Additional details are presented in depth in [1].

The second ML application related to DebrisSat is to minimize selection bias in the identification of thin DebrisSat fragments. As mentioned above, there is a known bias such that some metallic fragments are misidentified until the verification process can confirm the specific material based on the derived and measured quantities. This is a challenging, human-in-the-loop process that requires oversight and trained personnel to ensure the final assessment is accurate. Implementing a “dynamic volume” process and assuming ellipsoidal fragments appeared to constrain the volume calculations to the proper ranges for specific material types. The dynamic volume algorithm also helped assign mislabeled fragments to the appropriate density bins, as errors in volume calculations lead to erroneous material densities and thus incorrect material identifications. Details on processes and results for this application are available in [2].

In addition to DebrisSat, ML models have been developed to aid object detection in optical images from ES-MCAT. ES-MCAT is the ODPO's primary sensor used to statistically survey the geosynchronous orbit (GEO) region in order to characterize debris smaller than the sensitivity limit of the Space Surveillance Network (SSN). Detection of orbital debris in optical images generally involves humans manually reviewing images, along with the use of software algorithms to analyze images and identify detections that correspond to Earth-orbiting objects. ES-MCAT data is processed using the Observatory Control Software (OCS) to identify objects over a series of images [3]. Recently, ML models have been developed to assess performance for detecting debris in GEO survey images from ES-MCAT. A summary of this work is presented here, with more details to be discussed in a proposed paper intended for the upcoming 9th European Conference on Space Debris.

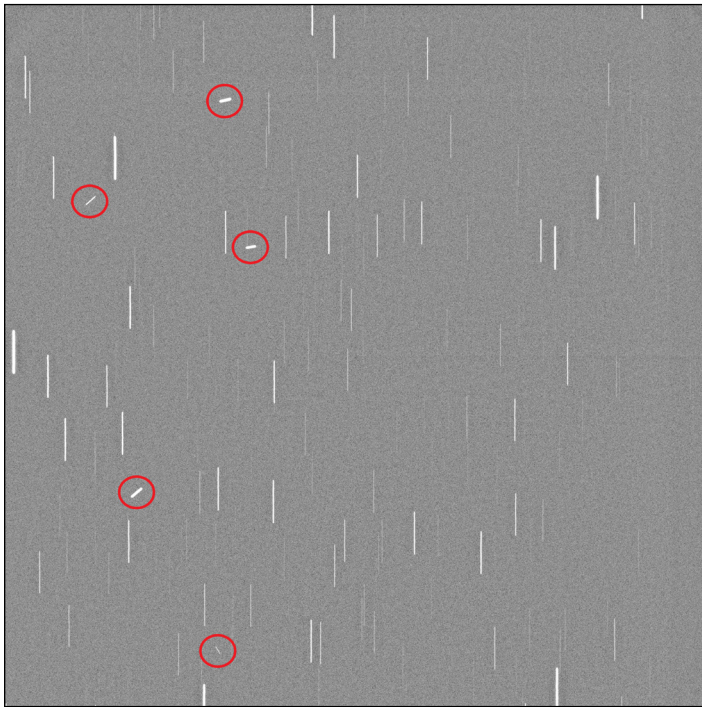


Figure 1. An example of a typical simulated object image used for the training model. The underlying image was taken using ES-MCAT on 8 February 2023. The long, vertically streaked objects are star trails. Of the 10 simulated objects used in the image, 5 are visible and circled in red, while the remaining 5 were too faint for human detection.

continued on page 3

ML Applications

continued from page 2

A predictive ML model is trained on data representative of telescope detections. For ES-MCAT GEO survey observations, detected objects appear as point sources or short streaks and stars appear as long streaks (see Figure 1). A limitation of using only real object detections is that the number of objects found with ES-MCAT over its survey durations is on the order of 100 objects, while an ML model would benefit from thousands of objects in order to train a robust and accurate object detection model. To expand on the data set of real detections and provide a large set of training data, the simulation capabilities of OCS were used. These can randomly generate any number of objects onto an image with random assigned streak lengths and magnitudes [4]. OCS simulations were run to generate 10 objects with any streak length between 0 and 4 arcseconds, random orientation, and a magnitude between 8-21. In total, OCS generated 5530 simulated objects. To ensure the model was trained on visible/real objects, the simulated objects were reviewed by humans. Since some simulated objects were too faint to be detected by humans or below the noise floor, only 4231 were available for model training and validation. Figure 1 shows a typical image with simulated objects.

The “You Only Look Once” version 9 (YOLOv9) architecture was used to train the ML model with these simulated objects. YOLOv9 [5] is a convolutional neural network (CNN) architecture that has a near state-of-the-art accuracy while also remaining fast to run in both train and inference modes. The original 4096x4096 TIFF images from ES-MCAT are first tiled into 16 1024x1024 PNG tiles. This is necessary because the objects are small relative to the size of the image, so the images could not be significantly resized during training. This also enables tiles to be shuffled during training and allows the dataset to more easily fit into GPU memory. The YOLOv9-C pretrained model was used for initialization. The model was trained with default hyperparameters with a batch size of 64 and image size of 1024. Once trained, the model can be run on new images for inference. With an RTX 5000 Ada laptop GPU, inference only takes 50 ms per tile, or 800 ms per full-size image. A typical detection of the ML model is given in Figure 2.

A comparison of the results using manual review of images, the OCS detection algorithm, and the ML model on GEO survey data from 2023 is given in the Table. With the ML model, 14 objects were discovered that were missed during manual review, a substantial improvement in identifying objects below the human detection threshold. Otherwise, the number of objects identified during manual review includes all objects detected by either ML or OCS, so that the total number of objects is the sum of the manual review number and the

14 faint objects. Even with these missed objects, manual review of the data still finds 95% of objects. The ML model finds 67% of the total objects in these data sets with the majority of missed objects being bright, overexposed point sources. Compared to OCS (53%), the ML model is a better detection method, but both computerized methods fall significantly below the manual review. If the two computer results are combined (removing any overlap of detected objects to avoid double counting), the percentage of total objects detected rises to 84%, a significant improvement over using one model alone. Additional model improvements can be attained by expanding the data set with additional images to improve the detection rates for objects underrepresented in the current simulated training data, or by building an ensemble of models.

continued on page 4

Table. Results from manual review, the OCS algorithm, and the new ML model for GEO survey data from 2023. The 194 objects for ML include 14 objects that were missed during manual review.

Set Name	Number of Objects	Percent of Total
Manual review	275 / 289	95%
OCS	154 / 289	53%
ML	194 / 289	67%
ML/OCS combined	244 / 289	84%
Total	289	--



Figure 2. An example of a typical detection by the ML model. This object was detected in data obtained on 7 March 2023. This object appears in only 2 images and the model finds the object each time. While the simulated data used to train the model does not have streaks with bright nodules throughout, as with this detection, the machine model can still accurately detect them.

ML Applications

continued from page 3

Finally, two potential applications of ML to orbital debris radar data collected with HUSIR and Goldstone are being investigated. First, the ODPO is exploring whether ML can predict orbital parameters for unknown objects using correlated objects as a “labeled dataset.” A second line of inquiry is whether ML can recognize changes in the debris population over time, including identifying new debris populations. Analysis of changes in the debris population currently relies on manual inspection of cumulative count rates and fluxes to determine regions of statistically significant changes.

ML applications to orbital debris research and analysis have the potential to greatly enhance and streamline the ability to characterize the orbital debris environment. Efforts are ongoing to understand the relative contributions and limitations for these applications and to ensure any models or tools developed provide robust and accurate results.

References

1. Siam, S., *et al.*, “Using Machine Learning to Infer Material Properties of Debris Fragments from X-ray Images in the DebrisSat

Project,” Second International Orbital Debris Conference, Houston, Texas, 2023.

2. Ondes, B., *et al.*, “NASA DebrisSat – Verification of Material Characterization Processes by Utilization of Machine Learning Algorithms.” Second International Orbital Debris Conference, Houston, Texas, 2023.

3. Hickson, P., “OCS: A Flexible Observatory Control System for Robotic Telescopes with Application to Detection and Characterization of Orbital Debris,” First International Orbital Debris Conference, Sugarland, TX (2019).

4. Hickson, P., *et al.* “Automated Detection and Analysis of Resident Space Objects with the 1.3-meter Eugene Stansberry-Meter Class Autonomous Telescope,” Second International Orbital Debris Conference, Sugarland, TX (2023).

5. Wang, C.-Y., *et al.* (2024). YOLOv9: Learning what you want to learn using programmable gradient information (arXiv:2402.13616). <http://arxiv.org/abs/2402.13616> ♦

Radar Measurements of the Orbital Debris Environment from HUSIR and Goldstone: 2023

A. MANIS AND J. A. HEADSTREAM

Statistical models developed by the NASA Orbital Debris Program Office (ODPO) to describe the orbital debris (OD) environment are built and validated using measurements

from specialized sensors capable of sampling objects too small to be tracked by the U.S. Space Surveillance Network (SSN). Ground-based radar measurements are the primary source of data on small debris in low Earth orbit (LEO), ranging in size from a few millimeters up to the sensitivity limit of the SSN. The Haystack Ultrawideband Satellite Imaging Radar (HUSIR), operated by the Massachusetts Institute of Technology’s Lincoln Laboratory (MIT/LL), provides data on debris with sizes down to approximately 5-7 mm at altitudes less than 1000 km and 2-3 cm throughout LEO. The Goldstone Orbital Debris Radar System (Goldstone), operated by NASA’s Jet Propulsion Laboratory (JPL), extends this coverage down to approximately 2 mm at 1000 km and below. This project review presents a summary of HUSIR and Goldstone detections in calendar year (CY) 2023. Detailed reports on these datasets are in work.

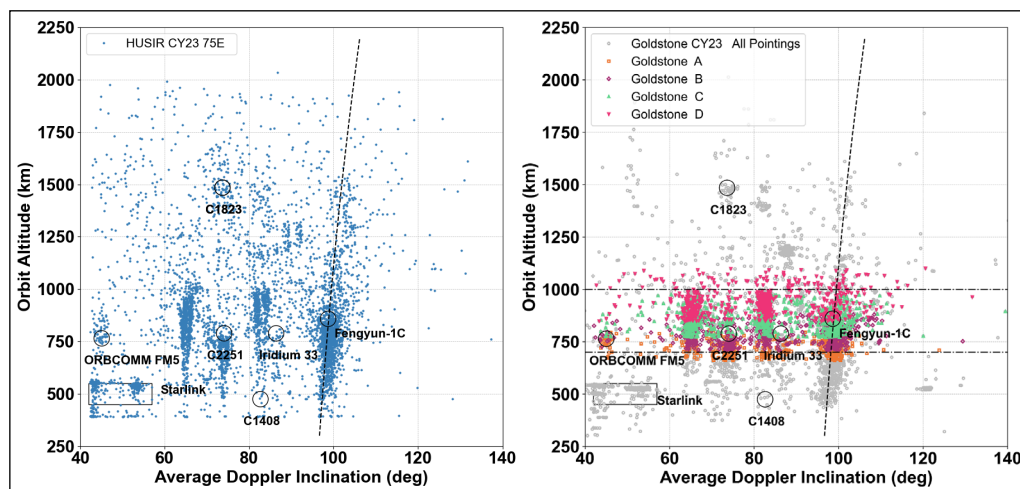


Figure 1. Orbit altitude versus average Doppler inclination for HUSIR (left) and Goldstone (right) 75E detections in CY 2023. Goldstone detections are differentiated by pointing with different colors and symbols. Gray points indicate detections outside a pointing’s main beam overlap, and the horizontal dashed lines denote the altitude region of interest covered by pointings A through D. The sun-synchronous condition, assuming a circular orbit, is indicated by the vertical dashed black lines. Notable debris clouds due to fragmentation events are highlighted with black circles, while detections associated with the Starlink constellation are encompassed by the black rectangle spanning 43-53° Doppler inclination.

For OD radar data collection, HUSIR and Goldstone operate in a beam park or staring mode and detect debris that pass through the radar beam. HUSIR typically operates

continued on page 5

Radar Measurements

continued from page 4

in three pointings: 75° elevation, due east (75E); 20° elevation, due south (20S); and 10° elevation, due south (10S). The bulk of the data is collected at the 75E pointing, and all HUSIR data presented here is from the 75E pointing. Goldstone is a bistatic radar, and for beam park observations, the transmitter is pointed at a fixed azimuth and elevation while the receiver is pointed to intersect the transmitter beam at a targeted slant range. In 2023, the ODPO used four pointings labeled “A,” “B,” “C,” and “D” to target specific altitudes of interest between 700 km and 1000 km [1].

The fundamental measurements made by the radar are range, range-rate (or Doppler velocity), and received power from which radar cross section (RCS) can be calculated. For developing models of the OD environment, parameters of interest include an object’s estimated orbit and size. Because of the short arc of an object’s path through the beam when operating in beam park mode, obtaining full orbital information with sufficient accuracy to construct precise orbits is not possible. By applying a circular orbit assumption, however, the range and range-rate can be converted to orbit altitude and inclination. The RCS is converted to a size using the NASA Size Estimation Model (SEM), which relates RCS to an object’s physical size based on laboratory RCS measurements [2, 3].

The orbit altitude versus average Doppler inclination from HUSIR and Goldstone detections in CY 2023 are shown in Figure 1. The Goldstone detections are differentiated by pointing for each pointing geometry, A through D, and gray points indicate detections from outside a pointing’s main beam overlap. Debris families are evident in this view and similar for both datasets. Notable on-orbit fragmentation events are also highlighted in Figure 1 with black circles. The circles are centered on the altitude and inclination of the parent body at the time of the event. A black rectangle outlines detections associated with the Starlink satellite constellation spanning approximately 43°–53° inclination. Starlink spacecraft also operate in orbits at 70° and between 97° and 98° inclination. While they do not contribute significantly enough to the detection rates at those altitudes and inclinations to be noticeable as separate populations in these figures, the evolution of their contributions will be monitored in the future. Fragments from the November 2021 Cosmos 1408 breakup near 500 km altitude and 82° inclination, which were prominent in the HUSIR CY 2022 data (ODQN vol. 27, issue 4, pp. 3-6), have mostly decayed and are no longer a significant population. Additional groupings, not labeled, correspond to the sodium-potassium (NaK) family near 65°, and a grouping near 900-1100 km altitude, 82° inclination, which has been identified in previous years and may correspond to a low-velocity shedding event [4].

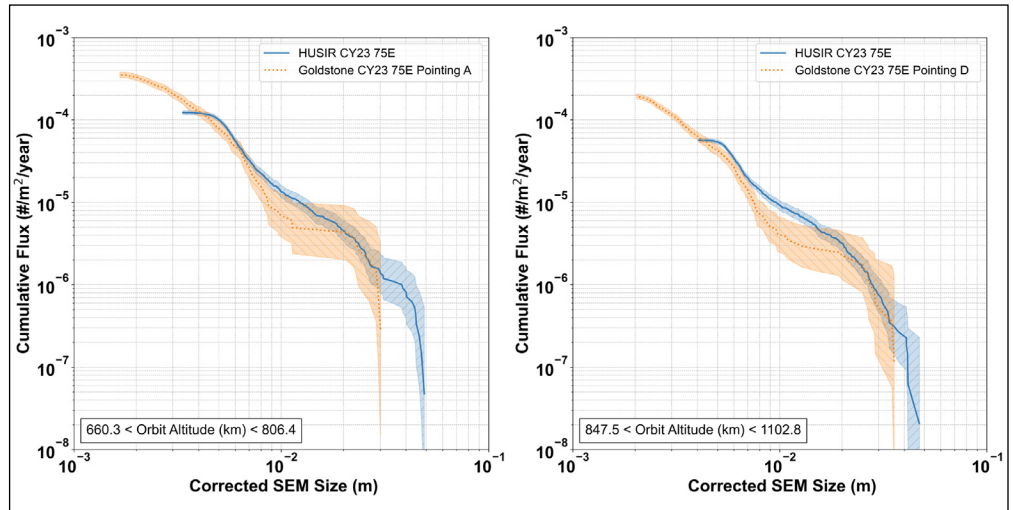


Figure 2. Cumulative flux versus SEM size comparisons for HUSIR and Goldstone in CY 2023, limited to the main beam overlap of Goldstone’s pointing A (left) and pointing D (right). The shaded regions represent the 2 σ uncertainty bounds.

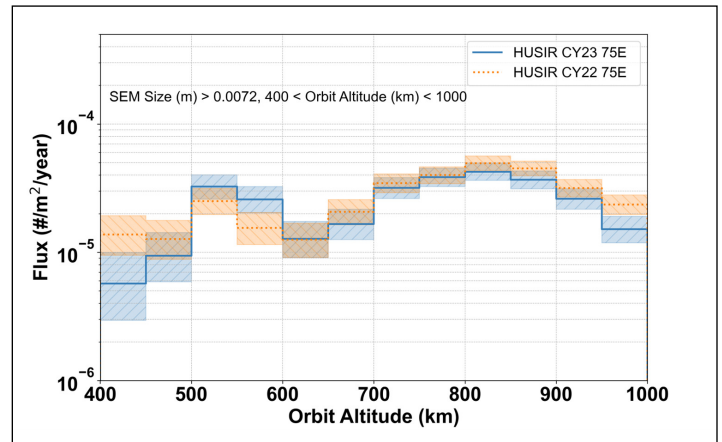


Figure 3. Surface area flux versus altitude limited to 7.2 mm for HUSIR 75E data in CY 2022 and CY 2023. The shaded regions represent the 2 σ uncertainty bounds.

Figure 2 compares the cumulative flux versus SEM size from HUSIR and Goldstone. HUSIR’s monostatic configuration covers a single range of LEO altitudes while Goldstone’s bistatic pointings provide coverage of specific altitudes where the transmitter and receiver beams overlap. Therefore, comparisons are made for specific altitude ranges corresponding to the main beam overlap of Goldstone’s pointing A (660.3 km to 806.4 km) and pointing D (847.5 km to 1102.8 km). These comparisons are also limited to sizes less than 5 cm to remove the effect of large intact objects. The flux is defined as the cumulative count rate for each sensor within the specified altitude range divided by the total lateral beam surface area between the minimum and maximum altitude defining that range. Goldstone’s sensitivity to smaller sizes compared to HUSIR is evident, with Goldstone extending

continued on page 6

Radar Measurements

continued from page 5

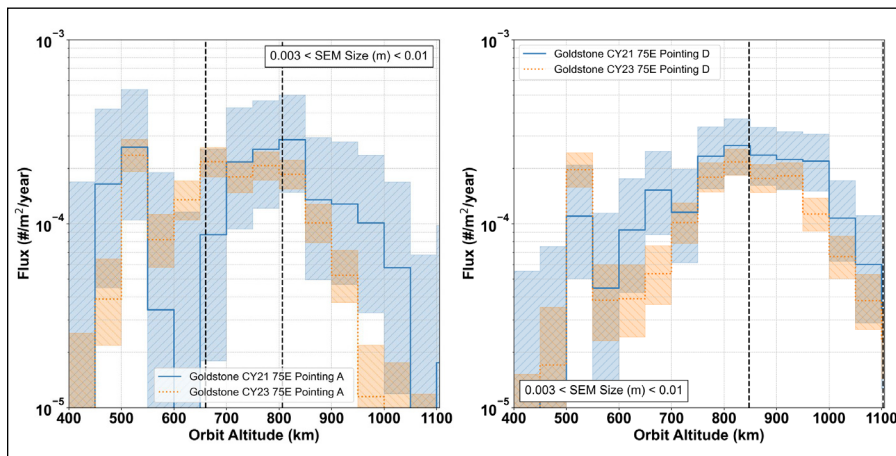


Figure 4. Surface area flux versus altitude limited to 3 mm for Goldstone pointing A (left) and pointing D (right) data in CY 2021 and CY 2023. Vertical dashed black lines represent the boundaries of the main beam overlap for each pointing. The shaded regions represent the 2σ uncertainty bounds.

the size coverage from HUSIR down to approximately 2-3 mm at these altitudes. At larger sizes, Goldstone is affected by saturation issues in the receiver; thus, the roll-off is at sizes around 1 cm for Goldstone detections. From the minimum completeness size of HUSIR to the larger roll-off size of Goldstone, the distributions from the two sensors overlap within their respective uncertainties.

A benefit of regular radar observations is the ability to look at variations in the population of small OD over time. The surface area flux as a function of orbit altitude, in 50 km bins, is shown in Figure 3 for HUSIR CY 2022 and CY 2023 detections. Because of variations in radar sensitivity from year to year, the flux is presented to a limiting size representing the completeness limit of the data for a given year. For HUSIR, flux is presented to a limiting SEM size of 7.2 mm. There is a slight increase from CY 2022 to CY 2023 in the 500-600 km altitude bins, which is attributable to the Starlink constellation spacecraft. A decrease in flux is observed at 400-500 km altitude, which is likely due to the rapid decay of debris generated by the Cosmos 1408 breakup. A statistically significant decrease is also observed at 950-1000 km altitude.

Figure 4 shows a comparison of Goldstone CY 2021 and CY 2023 surface area flux versus altitude for pointings A and D,

with CY 2022 omitted due to polarization issues that affected much of the data from that year (ODQN vol. 28, issue 1, pp. 3-5). Here, flux is presented for detections limited to an SEM size between 3 mm and 1 cm, with the upper limit imposed due to Goldstone's saturation issues at larger sizes. The vertical dashed black lines represent the upper and lower limits of the main beam overlap for each pointing. Within the main beam overlap, the fluxes are generally within their relative 2σ uncertainties. Outside the main beam overlap, significant increases at 500-550 km altitude are attributable to the Starlink constellation spacecraft. There also appears to be a decrease in flux at 950-1000 km altitude, as seen in the HUSIR data, that is only statistically significant in the main beam overlap of pointing D.

Regular radar measurements are essential for capturing year-to-year trends in the overall OD environment as well as the dynamic effects of individual breakup events. HUSIR and Goldstone continue to provide complementary data that enable a more robust characterization of the sub-centimeter LEO OD environment for updating the ODPO's OD models.

References

1. Arnold, J., *et al.* "Goldstone Radar Measurements of the Orbital Debris Environment: 2020-2021," NASA/TP-20240002199 (2024).
2. Handbook for Limiting Orbital Debris, NASA-Handbook 8719.14 (2008) https://standards.nasa.gov/sites/default/files/standards/NASA/Baseline/1/nasa-hdbk-871914_baseline_with_change_1.pdf Accessed 8 November 2024.
3. Xu, Y.-L., and Stokely, C. "A Statistical Size Estimation Model for Haystack and HAX Radar Detections." 56th International Astronautical Congress, Fukuoka, Japan (2005).
4. Gates, D., and Anz-Meador, P. "An 82 Degree Inclination Cloud Revealed by Radar." First International Orbital Debris Conference, Sugarland, TX, (2019). ♦

Subscribe to the ODQN or Update Your Subscription Information

To be notified by email when a new issue of the ODQN is placed online, or to update your personal information, please navigate to the ODQN subscription page on the NASA Orbital Debris Program Office (ODPO) website at: <https://orbitaldebris.jsc.nasa.gov/quarterly-news/subscription.cfm>. The ODPO respects your privacy. Your email address will be used solely for communication from the ODQN Managing Editor.

MEETING REPORTS

17-20 September 2024: 25th Advanced Maui Optical and Space Surveillance Technologies Conference (AMOS), Maui, Hawaii, USA

The 25th Advanced Maui Optical and Space Surveillance Technologies Conference (AMOS) was held in hybrid format 17-20 September 2024. This year's event hosted a total of 1101 attendees, with 231 joining virtually, including representatives from over 20 countries. The conference kicked off with a special presentation from the AMOS Conference Technical Chair, Paul Kervin, highlighting the evolution of conference topics since 1999, noting the orbital debris session is the longest running technical session since the inaugural conference. The opening keynote speaker was Lieutenant General Phillip A. Garrant, Commander Space Systems Command (SSC), United States Space Force (USSF). Lt. Gen. Garrant provided an historical overview of the changes in the space environment since the beginning of the space race, pivoting to space domain awareness (SDA) and the effects from breakups in orbit and anti-satellite tests, and addressed the need for more SDA in geosynchronous orbit (GEO).

The opening technical session for this year's conference was Space Debris, co-chaired by representatives from the NASA Orbital Debris Program Office (ODPO) and SSC. The NASA ODPO gave the first presentation on "Analysis of Darkened Fragments Resulting from Laboratory Hypervelocity Experiments," a joint research effort within the ODPO and NASA's Hypervelocity Impact Technology Team. Other topics presented in the Space Debris session included assessing resilience of low Earth orbit (LEO) constellations from fragmentation events; investigating end-of-life disposal strategies for cislunar missions; the evolution of sub-catalog space debris in high-altitude orbital regimes; and an overview of orbital debris space situational awareness (SSA) activities within NASA's Heliophysics Division. Additional orbital debris papers were presented as in-person and virtual posters, including targets for active debris removal; a comparison of NASA's Standard Satellite Breakup Model and Space Fence data; exploring soliton enhancement for ground-based detection of space debris; Poland's space law for mitigation and remediation of space debris; a feasibility study of spaceborne pulsed laser system for debris removal; DebrisSat error analysis; and deep learning applications for classifying space debris lightcurves.

The first day of the conference also featured a joint presentation on space logistics that drive SDA architecture

from Colonel Jeremy A. Raley, Director of the Space Vehicles Directorate within the Air Force Research Laboratory, and Col. Joseph J. Roth, Director of Innovation & Prototyping Acquisition Delta and Commander, SSC Detachment 1 within the USSF.

Dr. Hiroshi Yamakawa, President of the Japan Aerospace Exploration Agency (JAXA), provided the keynote address on day two of the conference. Dr. Yamakawa discussed space policy in Japan, highlighted several successful and upcoming missions and launches, spoke to various space situational facilities Japan operates, and provided information on future plans for active debris removal via commercial partnerships. The second day also included a featured presentation titled, "Victus Nox: Tactically Responsive Space – Space Domain Awareness Mission," presented by Lt. Col. Jason Altenhofen, USSF's SSC, and Gregory Less, Launch Systems Integration Manager with Millennium Space Systems.

On the last day, the keynote address was delivered by NASA Deputy Administrator Pam Melroy. As a former NASA astronaut, Melroy provided a thorough history of NASA's involvement with SSA, highlighting the ODPO, which has led the charge for space sustainability since 1979. The Deputy Administrator also announced a new organizational structure at headquarters to provide a unified front under the new Space Operations Mission Directorate, which will include a Space Sustainability Division led by the Director of Space Sustainability, Alvin Drew.

The final featured presentation focused on updates to the traffic coordination system for space, delivered by Richard DalBello, Director of the Office of Space Commerce at the National Oceanic and Atmospheric Administration (NOAA).

Three panels on SSA policy forums were held, one after each keynote address: "Sustainable Operations in the Space Environment: The Role of Orbital Carrying Capacity and Other Tools;" "SSA in the Asia-Pacific: Where We Are, Where We Are Going;" and "Space Weather and SSA – What's Needed Next?"

This year, five virtual short courses and nine additional in-person short courses were provided at the start of the conference.

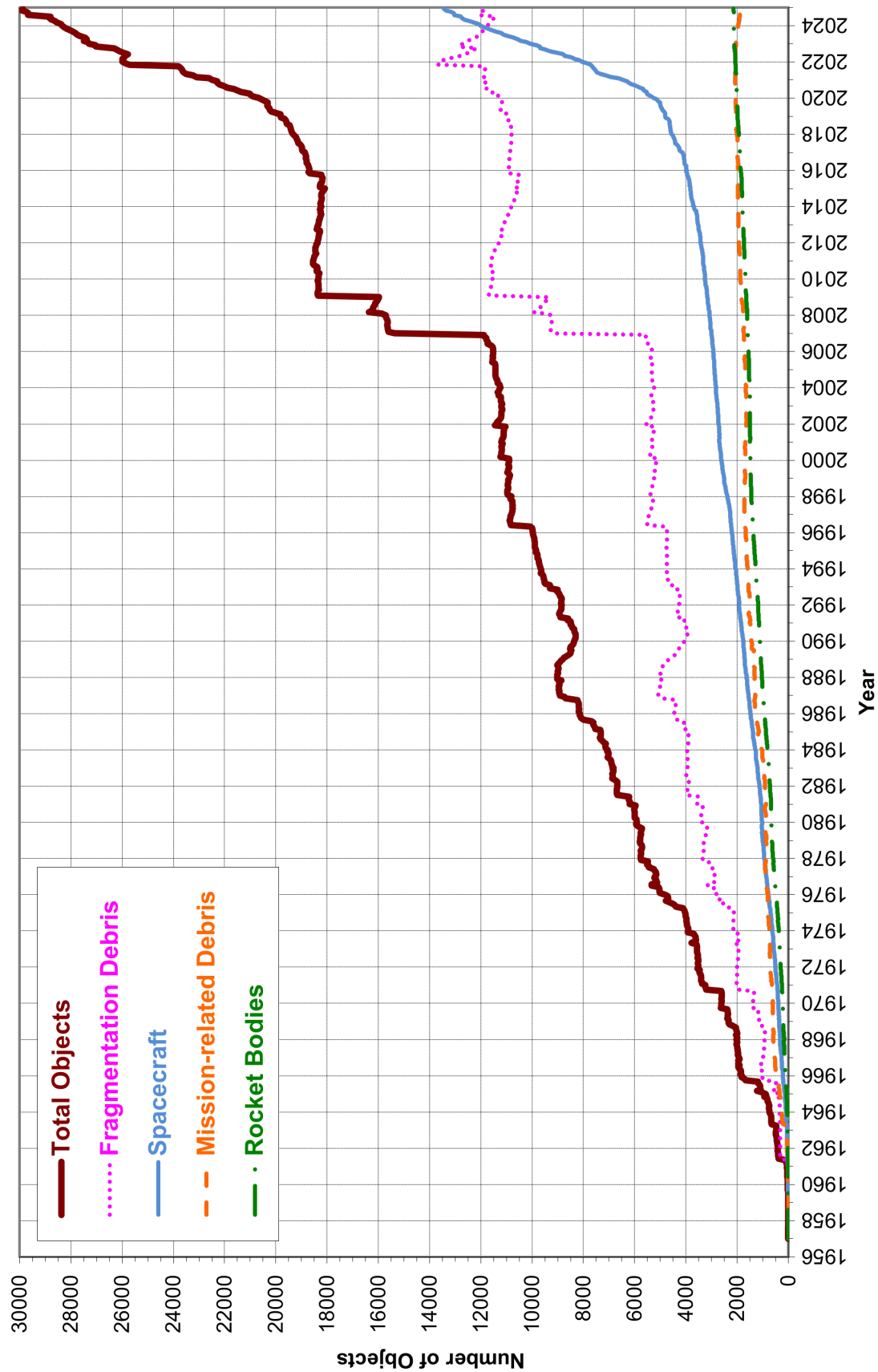
The next AMOS conference is scheduled for 16-19 September 2025. ♦

14-18 October 2024: 75th International Astronautical Congress (IAC), Milan, Italy

The 75th International Astronautical Congress (IAC) took place at the MICO Convention Center in Milan on 14-18 October 2024. Following the IAC tradition, the Space Debris Committee of the International Academy of Astronautics again organized a successful Space Debris Symposium during the IAC. More than 100 papers were presented in 10 debris sessions. Topics of the papers ranged from space situational awareness with radars and telescopes, environment modeling, orbital debris mitigation, active debris removal, and space sustainability, which reflected well with the main theme of the 2024 IAC: Responsible Space for Sustainability.

Many public and plenary events were organized during the IAC, including a special event entitled "One-to-One with Heads of Agencies." NASA Administrator Bill Nelson was one of the invited guests for the event. He described NASA's plan to return to the moon with international partners, the importance of the Artemis Accords, discoveries from the James Webb Space Telescope, asteroid deflection, and other major NASA activities. He also recalled his time in space as an astronaut on STS-51-D in 1985. ♦

Monthly Number of Objects in Earth Orbit by Object Type



Monthly Number of Cataloged Objects in Earth Orbit by Object Type as of 9 January 2025. This chart displays a summary of all objects in Earth orbit officially cataloged by the U.S. Space Surveillance Network. "Fragmentation debris" includes satellite breakup debris and anomalous event debris, while "mission-related debris" includes all objects dispensed, separated, or released as part of the planned mission.

UPCOMING MEETINGS

1-4 April 2025: 9th European Conference on Space Debris, Bonn, Germany

The 9th European Conference on Space Debris, hosted by the European Space Agency, will be held at the World Conference Center in Bonn, Germany. The conference provides a forum to discuss different aspects of space debris research, including measurements, environmental models, risk analysis techniques, protection designs, mitigation and remediation, and policy and regulation. Abstract submissions closed on 22 November 2024, but registration is still open. Additional details on the conference are available at: <https://space-debris-conference.sdo.esoc.esa.int/>.

29 September-3 October 2025: 76th International Astronautical Congress (IAC), Sydney, Australia

The 76th International Astronautical Congress (IAC) will be hosted by the Space Industry Association of Australia (SIAA) in Sydney, Australia, with a theme of "Sustainable Space: Resilient Earth," from 29 September to 3 October 2025. The International Academy of Astronautics (IAA) Space Debris Committee will again organize the Space Debris Symposium during the IAC. Ten debris sessions are planned on topics such as debris detection and tracking, environment modeling, mitigation, remediation, sustainability, and policy. The abstract submission deadline is 28 February 2025. Additional details of the 76th IAC are available at: <https://www.iac2025.org/>. ♦

INTERNATIONAL SPACE MISSIONS

1 August 2024 – 31 October 2024

continued on page 10

Intl.* Designator	Spacecraft	Country/ Organization	Perigee Alt. (KM)	Apogee Alt. (KM)	Inc. (DEG)	Addl. SC	Earth Orbital R/B	Other Cat. Debris
1998-067	ISS dispensed objects	Various	407	418	51.6	9	0	0
2024-135A	HG-02	PRC	35772	35803	0.0	0	1	0
2024-136A	STARLINK-31745	US	475	476	53.2	22	0	0
2024-137A	STRIX-4	JPN	526	536	43.0	0	2	0
2024-138A	STARLINK-32285	US	446	448	53.2	22	0	0
2024-139A	CYGNUS NG-21	US	407	418	51.6	0	0	0
2024-140A	QIANFAN-1	PRC	918	937	89.0	17	1	664
2024-141A	STARLINK-11228	US	359	361	53.2	20	0	0
2024-142A	CAPELLA-13 (ACADIA)	US	604	606	53.0	0	2	0
2024-143A	ASBM-1	NOR	8632	42960	62.4	0	1	0
2024-143B	ASBM-2	NOR	8636	42957	62.4			
2024-144A	STARLINK-32250	US	475	476	53.2	22	0	0
2024-145A	PROGRESS MS-28	CIS	407	418	51.6	0	1	0
2024-146A	LEGION 3	US	430	467	45.0	0	0	0
2024-146B	LEGION 4	US	697	704	45.0			
2024-147A	EOS-8	IND	453	462	37.4	1	2	0
2024-148A	YAOGAN-43 O1A	PRC	488	503	35.0	8	1	0
2024-149B	WARATAH SEED-1	AUS	503	508	97.4	112	0	0
2024-150A	STARLINK-31844	US	475	476	53.2	21	0	0
2024-151A	CHINASAT 4A	PRC	35774	35797	2.8	0	1	0
2024-152A	STARLINK-11247	US	359	360	53.2	20	0	0
2022-144K	USA 399	US	NO INITIAL ELEMENTS			0	0	0
2024-153A	OBJECT A	PRC	517	538	97.6	5	0	2
2024-154A	STARLINK-11242	US	359	360	53.2	20	0	0

SATELLITE BOX SCORE			
(as of 4 December 2024, cataloged by the U.S. SPACE SURVEILLANCE NETWORK)			
Country/ Organization	Spacecraft*	Spent Rocket Bodies & Other Cataloged Debris	Total
PRC	737	4810	5547
CIS	1558	5321	6879
ESA	101	27	128
FRANCE	100	531	631
INDIA	106	85	191
JAPAN	206	100	306
UK	717	1	718
USA	8709	4883	13592
OTHER	1139	97	1236
Total	13373	15855	29228


* active and defunct

Visit the NASA
Orbital Debris Program Office Website
<https://orbitaldebris.jsc.nasa.gov>

Technical Editor
Heather Cowardin, Ph.D.

Managing Editor
Ashley Johnson

Correspondence can be sent to:
Victoria Segovia
victoria.segovia@nasa.gov



National Aeronautics and Space Administration
Lyndon B. Johnson Space Center
2101 NASA Parkway
Houston, TX 77058
www.nasa.gov
<https://orbitaldebris.jsc.nasa.gov/>

INTERNATIONAL SPACE MISSIONS								
1 August 2024 – 31 October 2024								
continued from page 9								
Intl.* Designator	Spacecraft	Country/ Organiza- tion	Perigee Alt. (KM)	Apogee Alt.(KM)	Inc. (DEG)	Addl. SC	Earth Orbital R/B	Other Cat. Debris
2024-155A	STARLINK-11239	US	359	360	53.2	20	0	0
2024-156A	YAOGAN-43 02A	PRC	487	505	35.0	5	1	0
2024-157A	SENTINEL-2C	ESA	788	790	98.6	0	0	0
2024-158A	STARLINK-11278	US	130	137	53.2	20	0	0
2024-159A	GEESAT 3-01	PRC	578	598	50.0	9	0	0
2024-160A	USA 400	US	299	307	70.0	20	0	0
2024-161A	POLARIS DAWN	US	187	452	51.7	0	0	1
2024-162A	SOYUZ MS-26	CIS	407	418	51.6	0	1	0
2024-163A	SPACEMOBILE-003	US	503	521	53.0	4	0	0
2024-164A	STARLINK-11286	US	359	360	53.2	20	0	0
2024-165B	CHAMRAN-1	IRAN	540	559	64.1	0	1	1
2024-166A	OBJECT A	CIS	302	321	96.8	0	0	0
2024-166B	OBJECT B	CIS	302	321	96.8			
2024-167A	GALILEO 32 (137)	ESA	22865	22962	55.4	0	1	0
2024-167B	GALILEO 31 (10D)	ESA	23020	23215	55.4			
2024-168A	OBJECT A	PRC	21932	22384	54.9	0	1	1
2024-168B	OBJECT B	PRC	21527	22191	55.0			
2024-169A	OBJECT A	PRC	530	544	97.6	5	0	0
2024-170A	OBJECT A	PRC	853	861	44.9	3	1	0
2024-171A	STARLINK-11209	US	359	360	53.2	19	0	0
2024-172A	KINEIS-3C	FR	639	640	98.0	4	2	0
2024-173A	OBJECT A	PRC	473	488	97.4	7	1	2
2024-174A	OBJECT A	PRC	502	525	97.5	4	1	1
2024-175A	STARLINK-11300	US	359	360	53.2	19	0	0
2024-176A	IGS R-8	JPN	NO ELEMS. AVAILABLE			0	1	2
2024-177A	SJ-19	PRC	333	342	41.6	0	1	2
2024-178A	DRAGON FREEDOM-2	US	407	418	51.6	0	0	0
2024-179A	VULCAN CENTAUR R/B	US	492	498	30.0	0	0	0
2024-180A	HERA	ESA	HELIOCENTRIC					
2024-181A	HG-03	PRC	35778	35795	0.1	0	1	0
2024-182A	EUROPA CLIPPER	US	HELIOCENTRIC					
2024-183A	STARLINK-32174	US	418	419	53.2	22	0	0
2024-184A	STARLINK-11354	US	339	341	53.2	19	0	0
2024-185A	QIANFAN-19	PRC	837	853	89.0	17	1	0
2024-186A	GAOFEN 12-05	PRC	627	629	97.9	0	1	0
2024-187A	STARLINK-11356	US	340	340	53.2	19	0	0
2024-188A	ONEWEB-0015	US	615	624	86.6	19	0	0
2024-189A	OBJECT A	PRC	556	570	97.6	2	0	0
2024-190A	OBJECT A	PRC	494	500	35.0	2	1	0
2024-191A	STARLINK-32302	US	391	393	43.0	22	0	0
2024-192A	USA 421	US	480	485	70.0	16	0	0
2024-193A	STARLINK-32238	US	384	386	53.2	21	0	0
2024-194A	SZ-19	PRC	377	393	41.5	0	1	2
2024-195A	STARLINK-11335	US	324	325	53.2	19	0	0
2024-196A	STARLINK-32376	US	308	309	53.2	22	0	0
2024-197A	COSMOS 2579	CIS	497	506	97.6	0	1	0

Intl. = International; SC = Spacecraft; Alt. = Altitude; Inc. = Inclination; Addl. = Additional; R/B = Rocket Bodies; Cat. = Cataloged
Notes: 1. Orbital elements are as of data cut-off date 31 October. 2. Additional spacecraft on a single launch may have different orbital elements. 3. Additional uncatalogued objects may be associated with a single launch.